

Three-dimensional Anderson localization of light in dielectric disorder

Yevgen Grynko^{1*} and Jens Förstner²

¹BASF Coatings GmbH, Glasurit Str. 1, Münster, 48165, Germany.

²Theoretical Electrical Engineering, Institute for Photonic Quantum Systems, Paderborn University, Warburger Str. 100, Paderborn, 33098, Germany.

*Corresponding author(s). E-mail(s): yevgen.grynko@gmail.com;
Contributing authors: jens.foerstner@uni-paderborn.de;

Abstract

Strong localization of light in three-dimensional disordered dielectric systems remains challenging to establish because it requires extremely strong recurrent scattering, while the long-lived localized contribution can be weak and masked by diffusive leakage or absorption in finite samples. Here we use large-scale time-domain simulations to solve the full-vector Maxwell problem and investigate dense random packings of high-index dielectric particles deep in the late-time regime. As the early diffusive component escapes, the transmitted signal develops a non-exponential tail and an effective diffusion coefficient that decreases toward localized scaling. The late-time spectra consist of narrow, well-separated resonances with sub-unity Thouless conductance and approximately Poissonian spacing statistics, indicating weak spectral overlap between long-lived modes. Simultaneously, the near field fragments into compact, non-propagating intensity clusters separated by persistent low-intensity channels. Cycle-averaged maps show that this dark-channel network remains correlated over many optical periods, revealing a quasi-stationary confinement pattern. Together, the dynamical, spectral and real-space signatures provide converging evidence for Anderson-localized vector electromagnetic modes in a disordered three-dimensional dielectric medium. This convergence shows localization as a self-organization of the late-time field into interference-separated, landscape-like modal basins.

Keywords: disordered medium, light localization, light scattering

1 Introduction

Strong localization of electromagnetic waves in three-dimensional disordered media remains one of the most elusive problems in mesoscopic physics. First introduced by Anderson for electrons in random lattices [1], localization describes the breakdown of diffusion due to coherent multiple scattering and interference. Later it was demonstrated for other kinds of waves, in acoustics [2], quantum systems [3, 4], as well as 2D photonic [5–9] and microwave [10–12] structures. For light, this problem is especially challenging in 3D, where vector nature, near-field coupling, polarization mixing, and finite-size effects make the localization transition much harder to identify unambiguously than in lower-dimensional systems. Therefore, direct evidence for the strong localization of light in fully random 3D dielectric media remains controversial at present. Experimental claims of localization in strongly scattering powders [13–15] remain debated and have to be re-interpreted in the presence of absorption and inelastic processes [16–19].

Recent progress in high-performance computing and numerical time-domain methods for solving the Maxwell equations has revived the field by enabling large-scale 3D simulations deep into the late-time regime. In particular, first-principles simulations have shown clear 3D localization and an Anderson transition for vector electromagnetic waves in random ensembles of overlapping conducting spheres [20]. The same simulation framework reports an absence of localization for dielectric spheres even at very large index contrast, leaving the question of the 3D dielectric case open. At the same time, numerous studies have reported spatially confined optical states and transport anomalies consistent with localization in correlated 3D [21] and disordered 2D dielectric structures [5–8, 22]. These developments suggest that the absence of clear 3D evidence in dielectric systems may reflect not the impossibility of localization itself, but the difficulty of reaching and identifying the relevant regime.

In parallel, localization landscape (LL) theory has emerged as a powerful framework for describing wave confinement in complex media [23]. Originally developed for continuous media and scalar waves, it was later extended to discrete tight-binding [24] and 3D systems [25, 26]. The theory predicts a hidden static landscape (a foam-like surface in 3D) whose valleys partition a disordered structure into confinement subregions and govern the formation of localized states. In optics, this approach has proven successful in the 2D scalar field case [6]. An important implication of the theory is that the onset of localization can be associated with the formation of globally connected landscape barriers, suggesting a spatial criterion for a mobility edge [26].

Beyond its fundamental significance, 3D Anderson localization in dielectric media is attractive because disorder has already become a useful photonic resource in lower-dimensional systems. Localization-enabled confinement has been used to optimize random lasing [27], realize cavity quantum electrodynamics with disorder-induced modes in photonic-crystal waveguides [28], and develop concepts for optical sensing [29] and cavity optomechanics [30]. Extending such control to fully disordered 3D dielectric systems could open new opportunities in these areas. Importantly, strong localization could also provide an additional mechanism for controlling light dynamics in reservoir computing [31] and nonlinear photonic processing [32].

In this work, we use large-scale time-domain simulations to study light propagation through dense disordered particulate slabs composed of high-index dielectric particles. Going beyond transport-based diagnostics, we directly identify localization in real space within a fully 3D vector Maxwell system. Our results uncover a late-time regime in which long-lived confined near-field modes emerge together with the standard transport and spectral signatures associated with Anderson localization. This reveals the localized phase as a self-organization of the vector electromagnetic field into interference-separated, landscape-like modal basins.

2 Numerical model

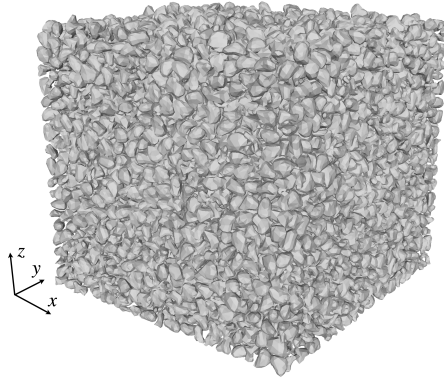


Fig. 1 Example of a unit cell with thickness $X_L = 16$ filled with 9000 irregular particles at volume fraction $\rho = 0.44$. The particles have refractive index $n = 3$ and characteristic size parameter $kr \approx 1$. The transverse directions XY are periodic, while the slab is open along the propagation direction Z.

We use the discontinuous Galerkin time-domain method (DGTD) [33] to solve the full-wave electromagnetic problem for systems of densely packed dielectric particles.

Previous work [34] showed that for particles with refractive index $n = 3$ and size parameter $kr \sim 1$ (k is the wavenumber and r the radius of the circumscribing sphere), progressive dense packing leads to a transition in transport observables at volume fractions $\rho > 0.4$, consistent with an approach to localization. This behavior was observed for granular samples with different sizes and boundary conditions, whereas lower-index or sparser systems remained diffusive. Here we use the same numerical setup and parameters and simulate light transmission by periodic monodisperse slabs with 6000-12000 non-overlapping particles with preserved granularity, mimicking a realistic powder (Fig. 1). Gaussian random field shapes are used as constituents [35–37]. The volume fraction is fixed at $\rho = 0.44$ and refractive index at $n = 3$. For the main study, we consider a unit cell with dimensions $X_d = 18$ (in size parameter units) along the X and Y axes and thickness $X_L = 16$ along Z, with $N = 9000$ particles and four disorder realizations. Additionally, we simulated transmission by samples with $X_L = 10.6$ and $X_L = 21.3$ to study the effect of layer thickness (Supplementary

material A.3). In all simulations, a model sample is illuminated by a short broadband E_x -polarized pulse propagating along the Z axis.

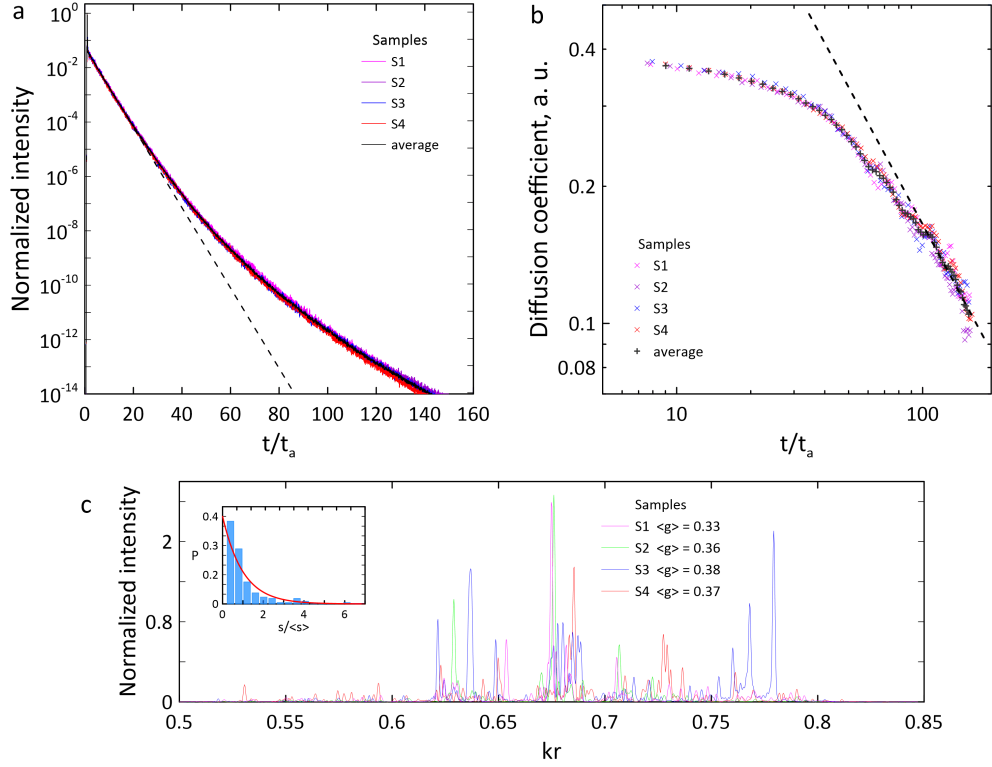


Fig. 2 Late-time transport slowdown and spectral isolation of long-lived modes. a, Time-resolved transmission $T(t)$ for four independent disorder realizations with slab thickness $X_L = 16$. After an initial diffusive interval, where the decay is close to exponential, all samples develop a pronounced non-exponential tail. The dashed line shows an exponential fit to the early-time regime. b, Effective decay rate $D(t)$ extracted by local exponential fitting of $T(t)$. The average $D(t)$ is obtained by fitting the $T(t)$ curve averaged over four samples. Individual realizations show step-like late-time variations, reflecting handovers between a limited number of long-lived quasi-modes with different leakage rates. Averaging over the four realizations suppresses these sample-specific crossovers and approaches the $1/t$ dependence (dashed line) expected for localized dynamics in an open system. c, Late-time ($t > 130t_a$) transmission spectra and Thouless conductances $\langle g \rangle$ measured for four samples. The horizontal axis is given in terms of the particle size parameter kr ; thus, the central wavelength of the excitation pulse corresponds to $kr = 1$. The spectra consist of narrow separated resonances concentrated in a reproducible interval $kr \simeq 0.62$ – 0.78 . The inset shows the normalized spacing distribution obtained by pooling the resonance spacings from all four spectra; its approximately Poissonian form is consistent with weakly overlapping localized modes.

3 Simulation results

We first study time-resolved transmission and track the changes in $T(t)$ and time-dependent diffusion coefficient $D(t)$ at longer times for four disordered samples. At sufficiently long observation times, we observe a qualitative transition in the transmission characteristics. Fig. 2a shows the emergence of a non-exponential tail in $T(t)$ after a diffusive period at early times characterized by an exponential dependence. The time scale is normalized by the pulse peak arrival time t_a . The effective decay rate $D(t)$ obtained by local exponential fitting of the $T(t)$ curves further confirms this transition (Fig. 2b). After $t \approx 40t_a$, $D(t)$ progressively becomes time- and sample-dependent. We note that the average $D(t)$ curve is deduced from the average $T(t)$ signal. The pronounced step-like variations of $D(t)$ observed for individual disorder realizations are strongly reduced after averaging and, at $t \gtrsim 100t_a$, the average $D(t)$ reaches the $1/t$ dependence in accordance with the analytical prediction for the localized regime [38].

Early-time $D(t)$ corresponds to the diffusive process, where self-averaging makes the integral transmission $T(t)$ nearly sample independent. At late times, after faster-decaying extended components have escaped, the signal is dominated by a limited number of long-lived, spatially confined quasi-modes with different leakage rates. Such modes are expected to produce an extended $D(t) \sim 1/t$ regime in the localized phase [20, 38]. In a finite sample, however, the number of contributing modes is small, so individual modal handovers can appear as step-like variations of $D(t)$. When one bright mode dominates the transmitted signal, the apparent decay rate may temporarily flatten or deviate from the asymptotic trend; after this contribution fades, the localized scaling is recovered. Averaging $T(t)$ over realizations mixes different modal lifetimes and coupling strengths, washing out these realization-specific crossovers and producing a smoother $D(t)$.

The late-time transmission spectra, evaluated after the decay of the initial transient regime ($t > 130t_a$), are in full agreement with this interpretation. They consist of well-resolved narrow resonances with strongly fluctuating amplitudes but comparatively similar linewidths (Fig. 2c). Remarkably, for four independent disorder realizations of the same sample thickness, the long-lived resonances are concentrated in nearly the same narrow spectral interval, $kr \simeq 0.62 - 0.78$, indicating a late-time spectral window in which leakage is minimized and spatial confinement is most efficient.

This behavior is consistent with modal localization in an open system. The linewidth of a localized resonance is mainly set by boundary leakage, which depends on confinement length, position within the slab, and hybridization with nearby modes. Although these factors vary between modes, they remain sufficiently similar within the late-time localized band to produce a relatively narrow distribution of decay rates. By contrast, resonance amplitudes depend on the overlap of each mode with the incident field and detection monitor. As localized modes occupy different regions in the bulk, this overlap fluctuates strongly, so modes with comparable lifetimes can have very different spectral weights.

The spectral isolation of the modes can be quantified using the Thouless conductance g [39], defined as the ratio of resonance linewidths to nearest-neighbor spacings, together with the level-spacing statistics. Here, we use a mean value $\langle g \rangle$ as an operational spectral-overlap parameter for the finite open system, not as a thermodynamic

finite-size-scaling conductance. For four independent realizations, the extracted values remain close, $\langle g \rangle = 0.33\text{--}0.38$, demonstrating that the system is in the weak-overlap regime $\langle g \rangle < 1$. The normalized spacing distribution $P(s/\langle s \rangle)$ obtained by pooling the spacings from all four spectra is shown in the inset of Fig. 2c. Its approximately Poissonian form is consistent with weakly interacting localized modes [40], in contrast to the level repulsion and Wigner-Dyson statistics expected for overlapping extended modes. Thus, the late-time spectral band, its reproducibility across independent samples, the sub-unity Thouless conductance, and the Poisson-like spacing statistics provide mutually consistent spectral evidence for a multimode localized regime.

For a consistency check, the transport parameter kl_{eff}^* (l_{eff}^* is the effective mean transport length for a given unit cell) for the diffusive component of the propagating field can be estimated from the slope of $\ln T(t)$ at early times when it follows the exponential law [41]. If s is the absolute value of the slope, with known slab thickness L , we can calculate the diffusion coefficient $D \approx L^2 s / \pi^2$. Using D and the effective refractive index $n_{eff} \approx 1.87$ the transport parameter becomes $kl_{eff}^* \approx 3kn_{eff}D/c \approx 1.21$. This satisfies the condition $kl^* \sim 1$ for the strong scattering regime [41–43]. However, we note that such an estimation is based on the averaged spectral content of the broadband pulse and, therefore, kl_{eff}^* is an effective broadband transport parameter here. If applied to localization, this condition should be considered as qualitative, which follows from the theoretical analysis [43] and experimental results, e.g., [8].

One can expect that a transition in transport characteristics is a result of the near field evolution leading to domination of long-lived modes. Fig. 3 shows representative instantaneous XZ intensity maps recorded at different times. Fig. 3a corresponds to the early times when $T(t)$ is exponential ($t \approx 10t_a$) and shows a randomly scattered distribution of the field hotspots as expected for classic diffusion. Fig. 3b corresponds to a transient pre-localized regime of small deviation of $T(t)$ from exponent and emerging structure in the near field ($t > 40t_a$). We previously observed similar behavior in smaller slabs with the same particle parameters and volume fraction [34]: randomly scattered hotspots tend to form structured patterns with time, reaching the stage with modes of increased lifetimes but remaining spatially overlapped. Here, we extended observation in larger samples to much longer times and reach a regime when persistent non-propagating resonant modes become spatially isolated at $t > 100t_a$ (Fig. 3c). This is a direct real-space signature of strong light localization. Fig. 3d shows a 3D representation of such a late-time near field. Application of a threshold filter to the high-intensity regions reveals a set of randomly distributed isolated blobs of nearly the same spatial scale (shown with red color). They correspond to the bright cores of the localized modes. A lower intensity background network is shown with the blue 3D contour. Interestingly, the number of bright non-overlapping modes typically seen in such instantaneous 3D snapshots is $\sim 30\text{--}50$, which is consistent with the approximate number of peaks in the transmission spectra. Here, the strongest transmission resonances correspond to a small modal subset that combines long lifetimes with efficient coupling to the external transmission channel, while many other localized modes remain weakly visible in the spectra despite being clearly present in the internal field. This dynamic picture can be seen in the field-map Videos 1 and 2 in the Supplementary material A.1.

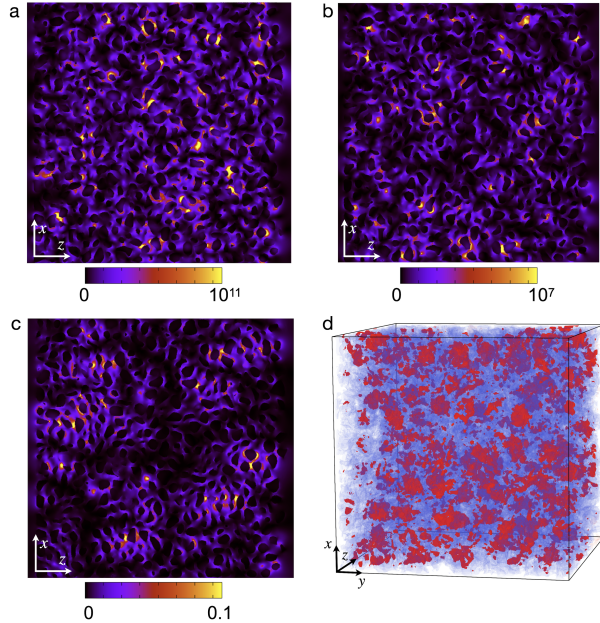


Fig. 3 Real-space emergence of spatially isolated late-time modes. a–c, Instantaneous near-field intensity ($|E|^2$) maps in the XZ plane at representative times. At early times ($t = 10t_a$), the field consists of randomly distributed hotspots characteristic of a diffusive multiple-scattering regime. At intermediate times ($t = 40t_a$), structured regions begin to emerge as the fastest extended components decay. At late times ($t = 140t_a$), the field breaks into compact, non-propagating intensity clusters separated by low-intensity regions, providing a direct real-space signature of strong localization of light. d, 3D rendering of the late-time near field. High-intensity thresholding reveals isolated modal cores (red), while a lower-intensity isosurface (blue) shows the surrounding weak field network. The number of visible compact modal regions is comparable to the number of late-time spectral peaks, indicating that the strongest transmission resonances represent only a subset of the localized quasi-modes present inside the slab.

Thus, the qualitative transitions observed in the near field are fully consistent with the changes in the integral transport observables, $T(t)$ and $D(t)$, as well as with the late-time transmission spectra. Taken together, and including the reproducibility for different slab thicknesses (Supplementary material A.3), these signatures provide consistent evidence for Anderson-localized electromagnetic modes in realistic disordered dielectric media. A precise determination of the mobility edge would require a dedicated finite-size scaling analysis [44, 45]; nevertheless, the simultaneous onset of anomalous long-time transport, spectrally isolated resonances, and spatially confined near-field patterns is consistent with entering a localized regime associated with a mobility-edge crossing.

At late times, the near field is no longer distributed diffusively, but breaks into spatially localized bright islands separated by persistent dark valleys. Measurements across several independently selected valleys, each averaged over 30–40 neighboring cuts, reveal a U-shaped barrier profile with similar width and minima levels at different locations (Fig. 4a), demonstrating that these minima are not accidental fluctuations.

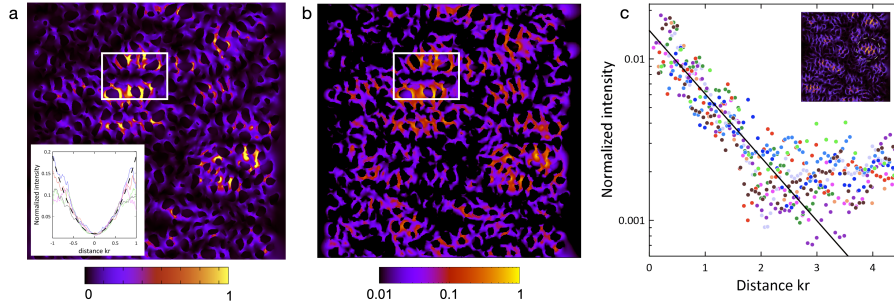


Fig. 4 Interference-defined barriers and compact modal decay. a, b, Late-time near-field intensity maps showing a close pair of bright localized regions separated by a dark valley, plotted on linear and logarithmic scales. The dark channel remains visible across a broad intensity range and does not simply follow particle-air interfaces, indicating that the mode boundary is defined by coherent field cancellation rather than by the material geometry alone. a, inset, Transverse profiles across five independently selected dark valleys, each averaged over neighboring cuts. The profiles have similar widths and minima levels and are approximately parabolic near the minima, consistent with smooth destructive-interference cancellation. The strong peak-to-valley contrast indicates weak coupling between adjacent bright basins. c, Average radial intensity profile for ten compact, comparatively isolated late-time modes. The inset shows an example of such a mode. The black line corresponds to an exponential fit. The common short-range exponential decay gives an effective near-field confinement length of $\xi \approx 0.7\lambda$ in free space, or $1.31\lambda_{eff}$ in the effective medium. This value characterizes the compact modal cores in the finite open system and provides an additional real-space indicator of strong confinement.

Even after averaging, the barrier contrast remains a factor of 10-20, while the local contrast between barrier minima and neighboring mode maxima exceeds two orders of magnitude (Fig. 4b). Such a strong and reproducible contrast is qualitatively consistent with LL-type confinement: it indicates that neighboring bright basins are separated by regions of strongly suppressed modal amplitude and weak coupling.

The transverse dark-valley profiles are approximately parabolic (Fig. 4a, inset), which is consistent with a local quadratic expansion around smooth destructive-interference minima. We interpret these valleys as regions of coherent field cancellation produced by the superposition of localized modes and residual background contributions. This interpretation is supported by their weak connection to the material geometry: rather than following particle-air interfaces, as expected for single-particle resonances, the dark channels often cut through dielectric material. The mode boundaries are therefore defined by the coherent field structure rather than by individual scatterers. The consistency of the approximately quadratic profiles supports the presence of an organized, LL-like barrier network whose detailed morphology remains frequency- and polarization-dependent.

An analysis of ten randomly selected comparatively isolated mode profiles shows that, despite noticeable mode-to-mode fluctuations, their short-range spatial decay follows a reproducible exponential trend (Fig. 4c). The scatter increases at larger distances, as expected because modal tails are more sensitive to the local disorder environment, residual overlap with neighboring resonances, and weak background contributions. We therefore use the common initial decay as an estimate of an effective

near-field confinement length of the modal cores, rather than as a scaling-theory localization length. A fit to the averaged decay gives $k\xi/2 \approx 2.21$ or $\xi \approx 0.7\lambda$ in free space and $1.31\lambda_{eff}$ for the effective wavelength in the medium. Although a more rigorous extraction would require spectrally isolated single-mode profiles and broader statistics, the reproducible exponential law provides an additional real-space indicator of a localized resonant regime. Wavelength-scale spatial decay of compact electromagnetic modes has also been reported in strongly scattering two-dimensional photonic and microwave systems [9, 10, 46, 47].

To quantify the persistence of the late-time field structure, we compute cycle-averaged field maps and their correlations (Supplementary material A.2). Fig. 5 shows XZ intensity maps averaged over 1–80 cycles. Increasing the averaging window suppresses phase-sensitive fluctuations while preserving the low-intensity regions. The corresponding correlations saturate after about 40 cycles and remain above 0.9 for 40–100-cycle averages (Fig. A.2), confirming that the confinement pattern is persistent on intermediate timescales. For averages separated by hundreds of cycles, the correlation decreases but remains well above the structural baseline, indicating partial preservation of the confinement network over much longer delays (Fig. A.3).

4 Discussion

The temporal persistence and large peak-to-valley contrast support an LL-like confinement picture and suggest a real-space mechanism for transport suppression: neighboring bright basins are separated by thin, high-contrast interference minima that strongly reduce modal coupling. In scalar LL theory, confinement is described through the landscape function u and the associated effective potential $W = 1/u$, whose high ridges partition the system into weakly coupled allowed regions [23]. The persistent low-intensity interfaces observed in the simulations play an analogous real-space role: they separate bright modal basins and strongly reduce modal overlap. In this sense, the LL concept of a mobility edge associated with a percolating barrier network [26] also becomes physically plausible for vector electromagnetic localization: the transition to long-lived confined modes would correspond to the formation of a connected low-intensity interface network that separates the field into weakly coupled basins.

Although our observations suggest that LL concepts remain physically meaningful in realistic 3D vector-wave media, a direct comparison requires a formulation appropriate for a vector field, where polarization, near-field coupling, and the vectorial structure of the electromagnetic operator can influence the effective confinement landscape. Our results therefore motivate a vector, polarization-resolved extension of LL theory for 3D dielectric media, which could provide a real-space criterion for the emergence of localized electromagnetic modes.

At this stage, we can formulate a general picture of the localization dynamics. Time filtering selects a small subset of long-lived quasi-modes whose coherent superposition produces persistent low-intensity and low-flux interfaces. In this regime, energy continues to leak from localized modes and through the open boundaries, but long-range internal transport is suppressed; energy decays locally rather than being carried

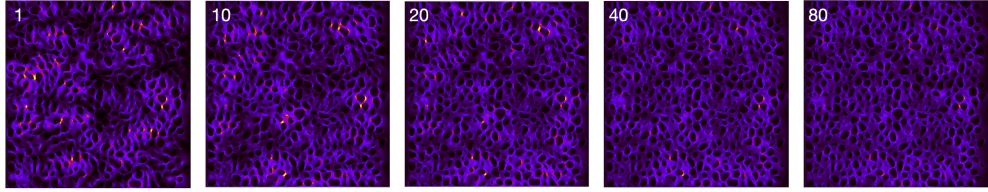


Fig. 5 Temporal persistence of the late-time confinement pattern. Late-time XZ near-field intensity maps at ($t = 140t_a$), averaged over progressively longer windows of 1–80 optical cycles. Increasing the averaging window suppresses phase-sensitive oscillations, while the same low-intensity regions remain visible. The persistence of the pattern under cycle averaging shows that the dark-channel network is not a transient speckle fluctuation, but a quasi-stationary confinement morphology shared by the long-lived modes. Quantitative correlations of these averaged maps are given in Supplementary Fig. A.2.

across the system. The relevant condition is therefore not merely strong disorder, but a strongly scattering and geometrically complex refractive-index environment. This is consistent with the broader view that transport in dense disordered photonic media is governed by local geometrical organization, short-range correlations, near-field coupling, and resonant neighborhoods [35, 48–51]. The precise role of wavelength-scale local complexity should be studied in future work through controlled comparisons of different geometrical models.

5 Conclusion

Our results show that strong localization of light in 3D dielectric disorder can be identified through a convergence of dynamical, spectral and real-space signatures. In the late-time regime, the decay of extended diffusive components exposes long-lived confined modes, non-exponential transmission, spectrally isolated resonances, and persistent low-intensity channels separating compact modal basins. These observations demonstrate that localization in a vector Maxwell system is not only a transport phenomenon, but also has a directly observable spatial morphology. The emergence of interference-separated, landscape-like confinement patterns suggests a route towards connecting time-resolved signatures of Anderson localization with real-space structure in disordered photonic media. More generally, the results indicate that dense dielectric disorder can support localized vector electromagnetic modes through the combined action of multiple scattering, near-field coupling and wavelength-scale geometrical complexity. This provides motivation for future experimental studies of 3D light localization in dielectric media.

Acknowledgments. The authors gratefully acknowledge the computing time granted by the Paderborn Center for Parallel Computing (PC²).

Methods. The numerical simulations were carried out with a self-developed light scattering code based on the open-source DGTD Maxwell solver MIDG published by Tim Warburton [52]. The code extends MIDG with material models, boundary conditions, and different light sources. Continuous and Gaussian pulses are supported. Plane-wave excitation is implemented using the total-field/scattered-field technique.

The computational domain is periodic in the transverse X and Y directions, and perfectly matched layers (PML) are applied in the longitudinal Z direction. For time-resolved transmission measurements, the sample layers are illuminated by a linearly polarized short plane-wave pulse propagating along Z. The transmitted intensity $T(t)$ is recorded in a monitor plane behind the layer, and all intensity curves are normalized by the peak intensity of the transmitted pulse.

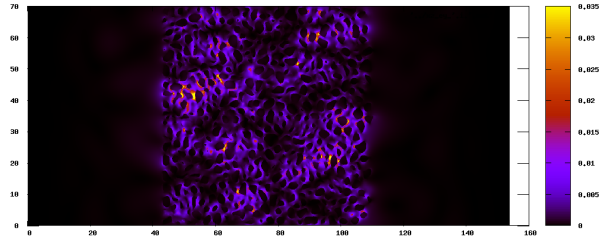
Particulate samples with different dimensions and controlled filling fractions were generated using the *Bullet* Physics engine [53], an open-source C++ library also available as a Blender add-on. It allows time-domain simulations of the dynamics and collisions of multiple arbitrary three-dimensional shapes, enabling the construction of powder-like samples with realistic topologies. Pre-generated random irregular particles were initially distributed sparsely and then allowed to settle freely under gravity onto a substrate inside a closed rectangular volume, forming slabs with controlled volume fraction. The particle shapes were produced with a self-developed generator based on the Gaussian random field approach. The resulting three-dimensional layer models were then used for tetrahedral mesh generation. In the dielectric regions with $n=3.0$, the spatial resolution was approximately 15 tetrahedral cells per central wavelength of the incident pulse, and the DGTD nodal expansion order was $N=3$. All DGTD simulations were performed on the Noctua 2 HPC cluster at Paderborn University.

A Supplementary material

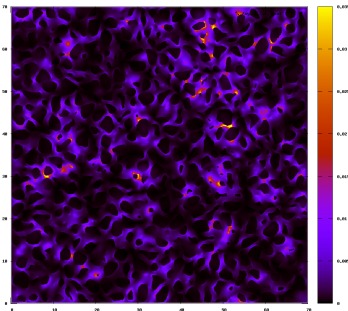
A.1 Late-time near field dynamics

In this section we present animated dynamics of the near field recorded for a sample with thickness $X_L = 16$ at late times ($t \approx 140t_a$) in the longitudinal, XZ, and transverse, XY, planes. Videos 1 and 2 show time evolution of the bright separated quasi-modes, each having its own eigenfrequency and spatial extent. The long-lived localized hotspot regions may temporarily fade and later reappear at the same spatial position. This behavior is consistent with beating between a small number of nearly degenerate localized quasi-modes. The confinement region itself remains pinned, while the local intensity is modulated by the evolving relative phases of the contributing modes populating it. Therefore, the underlying localized state is not destroyed, but becomes temporarily suppressed in intensity due to destructive interference within a weakly overlapping environment of long-lived modes.

The late-time videos also provide a qualitative check against significant reflections from the PML. The recorded XZ maps cover the full computational domain, including the regions between the slab and the absorbing boundaries. In a short-pulse simulation, any appreciable PML feedback would appear as delayed incoming wave fronts or extended boundary-related structures. Instead, Video 1 shows no waves returning from the absorbing layers toward the sample; the late-time field consists of compact resonances pinned inside the disordered slab. Together with the persistence of the same confined structures in the cycle-averaged maps (Figs. 5 and A.1), this supports their interpretation as intrinsic long-lived modes rather than boundary-reflection artifacts.



Video 1: Late-time near-field dynamics in XZ plane.



Video 2: Late-time near-field dynamics in XY plane.

A.2 Temporal persistence of the late-time confinement pattern

Here we analyze the long-time persistence of the near-field structure. Fig. A.1 shows YZ and XY intensity maps averaged over 1–80 cycles at $t \approx 140t_a$, displaying the same trend as the XZ maps in Fig. 5. This confirms that the quasi-stationary confinement network is not confined to a single cross-section, but reflects a three-dimensional field organization.

Fig. A.2 shows Pearson correlation coefficient calculated for different average maps with respect to the 100-cycle average. It increases monotonically with the averaging window in all three cross-section planes. For single-cycle maps the correlation is only about 0.65–0.70, indicating substantial instantaneous oscillatory or multimodal fluctuations. After averaging over 20–40 cycles, the correlation already exceeds approximately 0.85–0.93, and it approaches unity for 80–100 cycles. This shows that the late-time field has a stable underlying spatial morphology within the given time window.

One can also notice the persistence of distinct hotspots in two- or few-particle gaps even after averaging over about 100 optical cycles. This indicates the presence of exceptionally compact and long-lived resonant contributions. Such a behavior is physically plausible in a dense high-index random medium, where the most weakly leaking localized states may be supported by only a few strongly coupled particles. Such inter-particle gap resonances are, therefore, interpreted as the cores of the most prominent localized modes, while the surrounding weaker field averages out because it

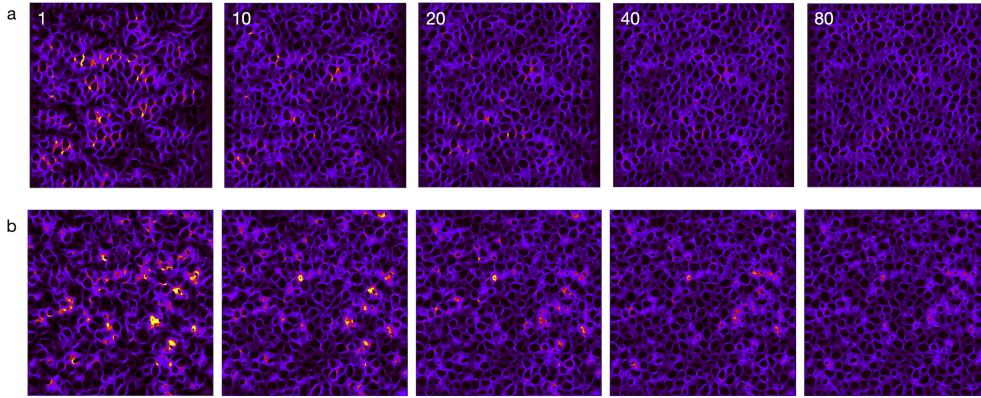


Fig. A.1 Three-dimensional persistence of the confinement pattern. Late-time near-field intensity maps in the YZ (a) and XY (b) planes, averaged over 1–80 optical cycles at $t = 140t_a$. The same trend as in the XZ plane is observed: cycle averaging suppresses fast phase-sensitive fluctuations while preserving extended low-intensity channels. This confirms that the quasi-stationary confinement pattern reflects a three-dimensional organization of the late-time field.

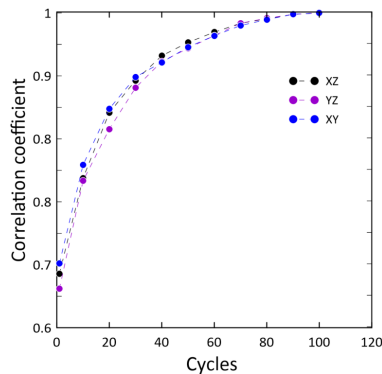


Fig. A.2 Correlation coefficient between cycle-averaged near-field maps and the corresponding 100-cycle average, calculated for XZ, YZ and XY cross-sections. The correlation increases monotonically with the averaging window in all planes. Single-cycle maps retain oscillatory and multimodal fluctuations, whereas averages over 20–40 cycles already reach correlations of approximately 0.85–0.93, approaching unity for 80–100 cycles. This behavior quantifies the emergence of a stable underlying confinement morphology after phase-sensitive fluctuations are averaged out.

is either less confined or less temporally stable. Thus, the granularity of the medium is an important part of the localization mechanism.

To assess the long-term stability of the pattern, we compute analogous cycle-averaged maps at an earlier time, $t \approx 120t_a$. Fig. A.3 shows that 45-cycle averages separated by about 360 optical cycles remain correlated. Although the maps do not show direct visual similarity, the dark regions in the difference maps point to areas that remain dark in both corresponding cycle-averaged field distributions (Figs. A.3a, d). The correlation coefficient between the maps at $t \approx 120t_a$ and $t \approx 140t_a$ is ≈ 0.79

for both the XZ and YZ planes, quantifying a persistent, though reduced, similarity of the confinement pattern.

We note that the fixed particle arrangement does contribute a nonzero baseline correlation, as confirmed by the comparison between an instantaneous snapshot and a 40-cycle average of the same realization, which typically yields correlation coefficients of only ≈ 0.3 . This provides an estimate of the purely static structural contribution. (Uncorrelated geometries like XZ and YZ cross-section give correlation coefficients of about 0.1-0.2). The substantially higher correlation obtained between two 45-cycle averages separated by a longer period, therefore, cannot be explained by the particle geometry alone and indicates the persistence of an additional field-organized pattern. That is, late-time field organization is not regenerated randomly, but retains a substantial sample-specific confinement pattern over long delays and does not imply a complete reorganization of the confinement structure, while the observed evolution is dominated by local redistribution of modal population.

These results are consistent with an interpretation in which a largely stationary disorder-defined confinement underlies the dynamics, while slower changes in modal occupation modify the apparent population of individual basins.

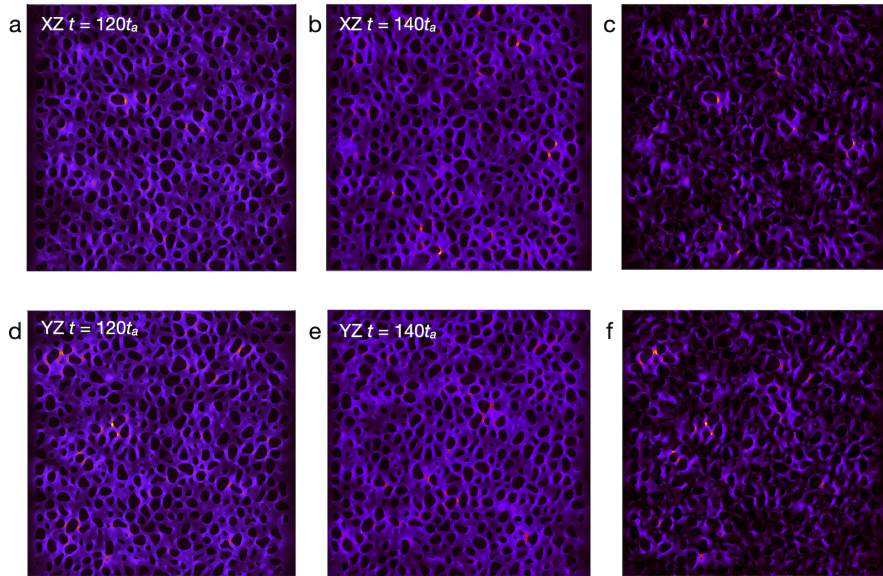


Fig. A.3 Long-delay persistence of the dark-channel pattern. a,b, XZ near-field intensity maps averaged over 45-cycle periods at $t \simeq 120t_a$ and $t \simeq 140t_a$, respectively. d,e, Corresponding YZ maps for the same two time windows. c,f, Unsigned difference maps for the XZ and YZ planes. Although the bright modal population changes over hundreds of optical cycles, extended dark regions remain partially preserved. The correlation between the two 45-cycle averages is approximately 0.79 in both planes, well above the structural baseline introduced by the static particle arrangement. This indicates that the late-time field is not regenerated randomly, but evolves within a persistent sample-specific confinement pattern.

A.3 Thickness dependence of late-time localization signatures

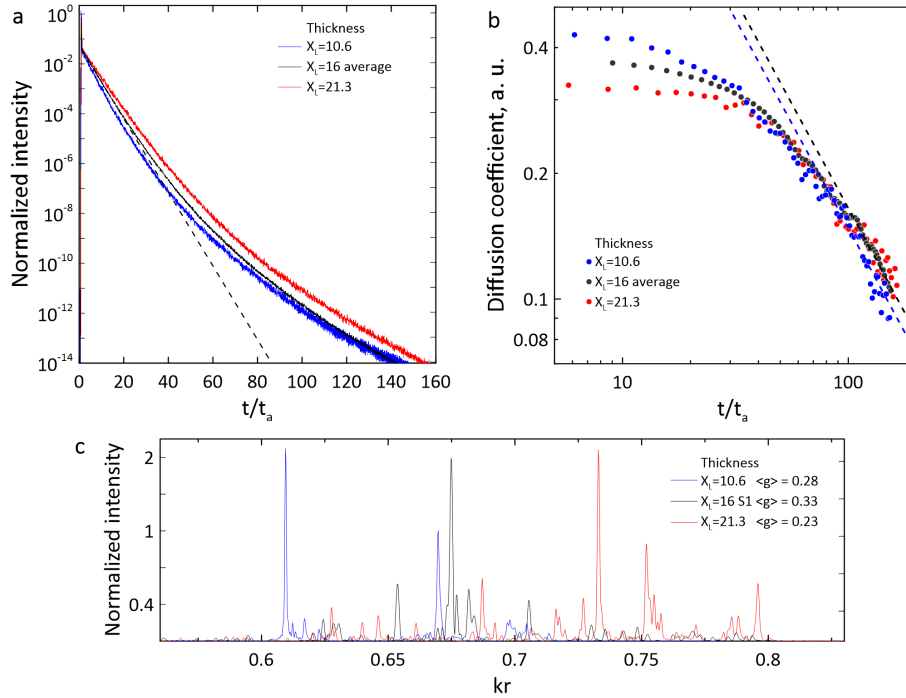


Fig. A.4 Thickness dependence of late-time transport and spectral signatures. a, Time-resolved transmission $T(t)$ for slabs with thicknesses $X_L = 10.6, 16$ (averaged), 21.3 , with the transverse dimensions kept fixed. All cases develop a non-exponential late-time tail, although the temporal onset depends on thickness because extended and diffusive components escape at different rates. b, Effective decay rate $D(t)$. The early-time values vary with slab thickness, as expected for different open-system leakage rates, but all curves show the same qualitative late-time slowdown toward localized-regime scaling. c, Late-time transmission spectra for the three thicknesses. The spectra contain narrow, well-separated resonances concentrated in the same spectral window, $kr \approx 0.62-0.8$. The mean Thouless conductances remain below unity for all thicknesses, indicating weak modal overlap. The small non-monotonic variation of $\langle g \rangle$ is attributed to finite-sample modal statistics rather than to a systematic thickness trend.

In this section, we test the effect of slab thickness by simulating layers thinner and thicker than those considered in the main text. The transverse dimensions are kept fixed, while the thicknesses are $X_L = 10.6$ and $X_L = 21.3$ with particle numbers $N = 6000$ and $N = 12000$, respectively. Fig. A.4a compares the corresponding transmissions $T(t)$ with the average curve from Fig. 2a. In all cases, a non-exponential tail emerges at long times, although the early-time decay rates $D(t)$ differ as expected for slabs of different thickness. Reducing slab thickness accelerates dynamical separation between rapidly escaping extended or diffusive components and long-lived spatially confined resonances. Once the slab remains several confinement lengths thick, localized cores can still be accommodated, while the open boundaries more efficiently suppress competing extended contributions. In thicker slabs, the larger volume supports more

slowly decaying diffuse modes, so the same late-time confined regime emerges only after longer time filtering. Thus, changing X_L mainly changes the time required for the extended background to leak out. Correspondingly, $D(t)$ shows the early-time variation with slab thickness, but all cases undergo the same qualitative late-time slowdown following the same downward trend toward the localized-regime scaling (Fig. A.4b).

The late-time spectra for all thicknesses consist of narrow, well-separated resonances concentrated in the same spectral window $kr \approx 0.62 - 0.8$ and the spectral structure remains qualitatively the same (Fig. A.4c). The extracted Thouless conductances, $\langle g \rangle = 0.28$ ($X_L = 10.6$) and $\langle g \rangle = 0.23$ ($X_L = 21.3$) are all below unity, indicating weak modal overlap for each thickness. This supports the interpretation that the long-lived resonances belong to the same localized spectral band and are not determined primarily by the slab thickness. The small non-monotonic variation of $\langle g \rangle$ is attributed to finite-sample modal statistics rather than a systematic thickness trend.

The near-field maps in Fig. A.5 show similar late-time confinement morphology for $X_L = 10.6$, $X_L = 16$ and $X_L = 21.3$. This indicates that the resonant structures are not set by the slab thickness, but by a local confinement scale in the dense medium. The finite slab therefore acts as an open-system temporal filter: rapidly escaping components disappear first, revealing long-lived resonances whose spatial extent remains nearly thickness independent. This test does not replace a full asymptotic scaling analysis, but it supports the interpretation that the observed modal isolation is a bulk property of the disordered medium, while residual finite-size and leakage effects remain present in the open system. We note that dedicated finite-size study would further refine the results by determining the asymptotic scaling behavior and locating the mobility edge. However, this would require ensemble averaging over many disorder realizations and several system sizes, making it nearly computationally prohibitive for the present full-wave 3D solution. Here, instead, we focus on the experimentally relevant finite open system and show that the late-time regime exhibits a converging set of localization signatures.

In addition, Fig. A.5 provides evidence that localization-like confinement morphology and interference-barrier networks can emerge on mesoscopic length scales of only a few confinement lengths. This does not require a macroscopically thick random medium or very long diffusive paths. Instead, it can be initiated locally by highly resonant complex scattering neighborhoods and then stabilized by surrounding destructive-interference valleys. This points to the importance of wavelength-scale geometrical complexity in the formation of the confinement landscape. Here, complexity means that the medium contains many distinct local scattering environments: narrow gaps, irregular particle shapes, locally resonant clusters, tortuous high-index/air interfaces, and a nontrivial network of possible field paths. Such local structure may promote stronger modal confinement than simpler random models based on spherical particles or point scatterers, even at comparable nominal disorder strength.

References

- [1] Anderson, P.W.: Absence of diffusion in certain random lattices. Phys. Rev. **109**, 1492–1505 (1958) <https://doi.org/10.1103/PhysRev.109.1492>

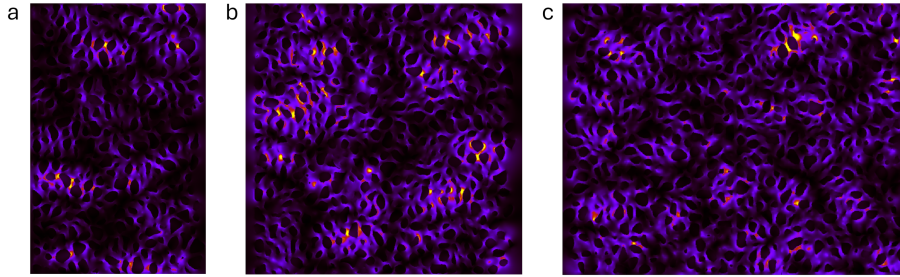


Fig. A.5 Late-time near-field XZ maps showing modal organization in slabs with different thicknesses, $X_L = 10.6$ (a), $X_L = 16$ (b) and $X_L = 21.3$ (c). The maps are taken at different times chosen such that $T(t) \sim 10^{-13}$ for each sample. Despite the change in longitudinal size, all cases display a similar organization into localized intensity clusters separated by extended low-intensity regions. This indicates that the characteristic confinement morphology is set mainly by local resonant scattering neighborhoods and interference barriers, rather than by the total slab thickness.

- [2] Hu, H., Strybulevych, A., Page, J.H., Skipetrov, S.E., Tiggelen, B.A.: Localization of ultrasound in a three-dimensional elastic network. *Nature Physics* **4**(12), 945–948 (2008)
- [3] Kondov, S.S., McGehee, W.R., Zirbel, J.J., DeMarco, B.: Three-dimensional anderson localization of ultracold matter. *Science* **334**(6052), 66–68 (2011)
- [4] Crespi, A., Osellame, R., Ramponi, R., Giovannetti, V., Fazio, R., Sansoni, L., De Nicola, F., Sciarrino, F., Mataloni, P.: Anderson localization of entangled photons in an integrated quantum walk. *Nature Photonics* **7**(4), 322–328 (2013)
- [5] Schwartz, T., Bartal, G., Fishman, S., Segev, M.: Transport and anderson localization in disordered two-dimensional photonic lattices. *Nature* **446**(7131), 52–55 (2007)
- [6] Shubitidze, T., Zhu, Y., Sundar, H., Negro, L.D.: Localization landscape of optical waves in multifractal photonic membranes. *Opt. Mater. Express* **14**(4), 1008–1024 (2024) <https://doi.org/10.1364/OME.520201>
- [7] Riboli, F., Barthelemy, P., Vignolini, S., Intonti, F., Rossi, A.D., Combrie, S., Wiersma, D.S.: Anderson localization of near-visible light in two dimensions. *Opt. Lett.* **36**(2), 127–129 (2011) <https://doi.org/10.1364/OL.36.000127>
- [8] Mondal, S., Kumar, R., Kamp, M., Mujumdar, S.: Optical thouless conductance and level-spacing statistics in two-dimensional anderson localizing systems. *Phys. Rev. B* **100**, 060201 (2019) <https://doi.org/10.1103/PhysRevB.100.060201>
- [9] Caselli, N., Intonti, F., La China, F., Biccari, F., Riboli, F., Gerardino, A., Li, L., Linfield, E.H., Pagliano, F., Fiore, A., Gurioli, M.: Near-field speckle imaging of light localization in disordered photonic systems. *Applied Physics Letters* **110**(8), 081102 (2017) <https://doi.org/10.1063/1.4976747>

- [10] Laurent, D., Legrand, O., Sebbah, P., Vanneste, C., Mortessagne, F.: Localized modes in a finite-size open disordered microwave cavity. *Phys. Rev. Lett.* **99**, 253902 (2007) <https://doi.org/10.1103/PhysRevLett.99.253902>
- [11] Aubry, G.J., Froufe-Pérez, L.S., Kuhl, U., Legrand, O., Scheffold, F., Mortessagne, F.: Experimental tuning of transport regimes in hyperuniform disordered photonic materials. *Phys. Rev. Lett.* **125**, 127402 (2020) <https://doi.org/10.1103/PhysRevLett.125.127402>
- [12] Dalichaouch, R., Armstrong, J.P., Schultz, S., Platzman, P.M., McCall, S.L.: Microwave localization by two-dimensional random scattering. *Nature* **354**(6348), 53–55 (1991) <https://doi.org/10.1038/354053a0>
- [13] Wiersma, D.S., Bartolini, P., Lagendijk, A., Righini, R.: Localization of light in a disordered medium. *Nature* **390**(6661), 671–673 (1997) <https://doi.org/10.1038/37757>
- [14] Störzer, M., Gross, P., Aegerter, C.M., Maret, G.: Observation of the critical regime near anderson localization of light. *Phys. Rev. Lett.* **96**, 063904 (2006) <https://doi.org/10.1103/PhysRevLett.96.063904>
- [15] Sperling, T., Bührer, W., Aegerter, C.M., Maret, G.: Direct determination of the transition to localization of light in three dimensions. *Nature Photonics* **7**(1), 48–52 (2013) <https://doi.org/10.1038/nphoton.2012.313>
- [16] Scheffold, F., Lenke, R., Tweer, R., Maret, G.: Localization or classical diffusion of light? *Nature* **398**(6724), 206–207 (1999) <https://doi.org/10.1038/18347>
- [17] Scheffold, F., Wiersma, D.: Inelastic scattering puts in question recent claims of anderson localization of light. *Nature Photonics* **7**(12), 934–934 (2013) <https://doi.org/10.1038/nphoton.2013.210>
- [18] Sperling, T., Schertel, L., Ackermann, M., Aubry, G.J., Aegerter, C.M., Maret, G.: Can 3d light localization be reached in ‘white paint’? *New Journal of Physics* **18**(1), 013039 (2016) <https://doi.org/10.1088/1367-2630/18/1/013039>
- [19] Skipetrov, S.E., Page, J.H.: Red light for anderson localization. *New Journal of Physics* **18**(2), 021001 (2016) <https://doi.org/10.1088/1367-2630/18/2/021001>
- [20] Yamilov, A., Skipetrov, S.E., Hughes, T.W., Minkov, M., Yu, Z., Cao, H.: Anderson localization of electromagnetic waves in three dimensions. *Nature Physics* **19**(9), 1308–1313 (2023)
- [21] Haberko, J., Froufe-Pérez, L.S., Scheffold, F.: Transition from light diffusion to localization in three-dimensional amorphous dielectric networks near the band edge. *Nature Communications* **11**(1), 4867 (2020)

- [22] Conley, G.M., Burrelli, M., Pratesi, F., Vynck, K., Wiersma, D.S.: Light transport and localization in two-dimensional correlated disorder. *Phys. Rev. Lett.* **112**, 143901 (2014) <https://doi.org/10.1103/PhysRevLett.112.143901>
- [23] Filoche, M., Mayboroda, S.: Universal mechanism for anderson and weak localization. *Proceedings of the National Academy of Sciences* **109**(37), 14761–14766 (2012) <https://doi.org/10.1073/pnas.1120432109> <https://www.pnas.org/doi/pdf/10.1073/pnas.1120432109>
- [24] Lyra, M. L., Mayboroda, S., Filoche, M.: Dual landscapes in anderson localization on discrete lattices. *EPL* **109**(4), 47001 (2015) <https://doi.org/10.1209/0295-5075/109/47001>
- [25] Skipetrov, S.E.: Higher-order localization landscape theory of anderson localization. *Phys. Rev. B* **110**, 214209 (2024) <https://doi.org/10.1103/PhysRevB.110.214209>
- [26] Filoche, M., Pelletier, P., Delande, D., Mayboroda, S.: Anderson mobility edge as a percolation transition. *Phys. Rev. B* **109**, 220202 (2024) <https://doi.org/10.1103/PhysRevB.109.L220202>
- [27] Rashidi, M., Li, Z., Jagadish, C., Mokkalapati, S., Tan, H.H.: Controlling the lasing modes in random lasers operating in the anderson localization regime. *Opt. Express* **29**(21), 33548–33557 (2021) <https://doi.org/10.1364/OE.441003>
- [28] Vasco, J.P., Hughes, S.: Anderson localization in disordered In photonic crystal slab cavities. *ACS Photonics* **5**(4), 1262–1272 (2018) <https://doi.org/10.1021/acsp Photonics.7b00967>
- [29] Trojak, O.J., Crane, T., Sapienza, L.: Optical sensing with anderson-localised light. *Applied Physics Letters* **111**(14), 141103 (2017) <https://doi.org/10.1063/1.4999936>
- [30] Arregui, G., Ng, R.C., Albrechtsen, M., Stobbe, S., Sotomayor-Torres, C.M., García, P.D.: Cavity optomechanics with anderson-localized optical modes. *Phys. Rev. Lett.* **130**, 043802 (2023) <https://doi.org/10.1103/PhysRevLett.130.043802>
- [31] Rafayelyan, M., Dong, J., Tan, Y., Krzakala, F., Gigan, S.: Large-scale optical reservoir computing for spatiotemporal chaotic systems prediction. *Physical Review X* **10**, 041037 (2020) <https://doi.org/10.1103/PhysRevX.10.041037>
- [32] Wang, H., Hu, J., Morandi, A., Nardi, A., Xia, F., Li, X., Savo, R., Liu, Q., Grange, R., Gigan, S.: Large-scale photonic computing with nonlinear disordered media. *Nature Computational Science* **4**(6), 429–439 (2024) <https://doi.org/10.1038/s43588-024-00644-1>
- [33] Hesthaven, J.S., Warburton, T.: Nodal high-order methods on unstructured grids:

- I. time-domain solution of maxwell's equations. *Journal of Computational Physics* **181**(1), 186–221 (2002) <https://doi.org/10.1006/jcph.2002.7118>
- [34] Grynko, Y., Siebert, D., Sperling, J., Förstner, J.: 3d anderson localization of light in disordered systems of dielectric particles. <https://arxiv.org/abs/2312.14393> (2023) [arXiv:2312.14393](https://arxiv.org/abs/2312.14393) [physics.optics]
- [35] Grynko, Y., Shkuratov, Y., Förstner, J.: Light backscattering from large clusters of densely packed irregular particles. *Journal of Quantitative Spectroscopy and Radiative Transfer* **255**, 107234 (2020) <https://doi.org/10.1016/j.jqsrt.2020.107234>
- [36] Grynko, Y., Shkuratov, Y., Alhaddad, S., Förstner, J.: In: Kokhanovsky, A. (ed.) *Light Scattering by Large Densely Packed Clusters of Particles*, pp. 125–155. Springer, Cham (2022). https://doi.org/10.1007/978-3-031-10298-1_4 . https://doi.org/10.1007/978-3-031-10298-1_4
- [37] Grynko, Y., Shkuratov, Y., Förstner, J.: Intensity surge and negative polarization of light from compact irregular particles. *Opt. Lett.* **43**(15), 3562–3565 (2018)
- [38] Skipetrov, S.E., Tiggelen, B.A.: Dynamics of anderson localization in open 3d media. *Phys. Rev. Lett.* **96**, 043902 (2006) <https://doi.org/10.1103/PhysRevLett.96.043902>
- [39] Thouless, D.J.: Electrons in disordered systems and the theory of localization. *Physics Reports* **13**(3), 93–142 (1974) [https://doi.org/10.1016/0370-1573\(74\)90029-5](https://doi.org/10.1016/0370-1573(74)90029-5)
- [40] Escalante, J.M., Skipetrov, S.E.: Level spacing statistics for light in two-dimensional disordered photonic crystals. *Scientific Reports* **8**(1), 11569 (2018) <https://doi.org/10.1038/s41598-018-29996-1>
- [41] Lagendijk, A., van Tiggelen, B.A.: Resonant multiple scattering of light. *Physics Reports* **270**(3), 143–215 (1996) [https://doi.org/10.1016/0370-1573\(95\)00065-8](https://doi.org/10.1016/0370-1573(95)00065-8)
- [42] Ioffe, A.F., Regel, A.R.: In: Gibson, A.F. (ed.) *Non-crystalline, amorphous, and liquid electronic semiconductors*, vol. 4, pp. 237–291. Wiley, New York (1960)
- [43] Skipetrov, S.E., Sokolov, I.M.: Ioffe-regel criterion for anderson localization in the model of resonant point scatterers. *Phys. Rev. B* **98**, 064207 (2018) <https://doi.org/10.1103/PhysRevB.98.064207>
- [44] Abrahams, E., Anderson, P.W., Licciardello, D.C., Ramakrishnan, T.V.: Scaling theory of localization: Absence of quantum diffusion in two dimensions. *Physical Review Letters* **42**, 673–676 (1979) <https://doi.org/10.1103/PhysRevLett.42.673>
- [45] MacKinnon, A., Kramer, B.: One-parameter scaling of localization length and

- conductance in disordered systems. *Physical Review Letters* **47**, 1546–1549 (1981) <https://doi.org/10.1103/PhysRevLett.47.1546>
- [46] Razo López, L.A.: Localization of electromagnetic waves beyond anderson: Role of correlations, symmetries and topology. Phd thesis, Université Côte d’Azur, Nice, France (2024). NNT: 2024COAZ5013. <https://theses.hal.science/tel-04633536v1>
- [47] Shi, X., Chen, X., Malomed, B.A., Panoiu, N.C., Ye, F.: Anderson localization at the subwavelength scale for surface plasmon polaritons in disordered arrays of metallic nanowires. *Phys. Rev. B* **89**, 195428 (2014) <https://doi.org/10.1103/PhysRevB.89.195428>
- [48] Vynck, K., Pierrat, R., Carminati, R., Froufe-Pérez, L.S., Scheffold, F., Sapienza, R., Vignolini, S., Sáenz, J.J.: Light in correlated disordered media. *Rev. Mod. Phys.* **95**, 045003 (2023) <https://doi.org/10.1103/RevModPhys.95.045003>
- [49] Schertel, L., Siedentop, L., Meijer, J.-M., Keim, P., Aegerter, C.M., Aubry, G.J., Maret, G.: The structural colors of photonic glasses. *Advanced Optical Materials* **7**(15), 1900442 (2019) <https://doi.org/10.1002/adom.201900442> <https://advanced.onlinelibrary.wiley.com/doi/pdf/10.1002/adom.201900442>
- [50] Aubry, G.J., Schertel, L., Chen, M., Weyer, H., Aegerter, C.M., Polarz, S., Cölfen, H., Maret, G.: Resonant transport and near-field effects in photonic glasses. *Phys. Rev. A* **96**, 043871 (2017) <https://doi.org/10.1103/PhysRevA.96.043871>
- [51] Rezvani Naraghi, R., Sukhov, S., Sáenz, J.J., Dogariu, A.: Near-field effects in mesoscopic light transport. *Phys. Rev. Lett.* **115**, 203903 (2015) <https://doi.org/10.1103/PhysRevLett.115.203903>
- [52] Warburton, T.: Mini Discontinuous Galerkin Maxwells Time-domain Solver. <https://github.com/tcew>
- [53] Coumans, E., Bai, Y.: PyBullet, a Python module for physics simulation for games, robotics and machine learning. <http://pybullet.org> (2016–2021)